Chinese Chemical Letters 35 (2024) 109626

Contents lists available at ScienceDirect

Chinese Chemical Letters

journal homepage: www.elsevier.com/locate/cclet

Fe(III)-juglone nanoscale coordination polymers for cascade chemodynamic therapy through synergistic ferroptosis and apoptosis strategy

Zhendong Liu[a,b], Sainan Liu[a], Bin Liu[c], Qi Meng[a,b], Meng Yuan[a,b], Chunzheng Yang[a,b], Yulong Bian[a,b], Ping'an Ma[a,b,*], Jun Lin[a,b,*]

[a] State Key Laboratory of Rare Earth Resource Utilization, Changchun Institute of Applied Chemistry, Chinese Academy of Sciences, Changchun 130022, China
[b] School of Applied Chemistry and Engineering, University of Science and Technology of China, Hefei 230026, China
[c] College of Materials Science and Chemical Engineering, Harbin Engineering University, Harbin 150001, China

ARTICLE INFO

Article history:
Received 7 December 2023
Revised 31 January 2024
Accepted 3 February 2024
Available online 13 February 2024

Keywords:
Nanoscale coordination polymers
Juglone
Tumor microenvironment
Enhanced chemodynamic therapy
Ferroptosis

ABSTRACT

Chemodynamic therapy (CDT) relying on the transformation of endogenous hydrogen peroxide (H_2O_2) into cytotoxic hydroxyl radicals (·OH) based on the catalysis of Fenton/Fenton-type reactions exhibits great potentiality for cancer treatment. However, the inadequate H_2O_2 supply and intricate redox homeostasis in tumor microenvironment (TME) severely impair the efficacy of CDT. Herein, we design self-assembled 1,2-distearoyl-*sn*–glycero-3-phosphoethanolamine conjugated polyethylene glycol (DSPE-PEG)-modified Fe(III)-juglone nanoscale coordination polymers (FJP NCPs) as redox homeostasis disruptors for juglone-enhanced CDT. Responding to glutathione (GSH)-rich and acidic TME, the Fe^{2+}/Fe^{3+}-guided CDT and GSH consumption by Fe^{3+} are activated, resulting in ·OH downstream and up-regulation of lipid peroxidation (LPO). In addition, the released juglone not only depletes GSH through Michael addition, but also elevates intracellular H_2O_2 level for achieving ·OH further bursting. With the impressive efficiency of GSH exhaustion and reactive oxygen species (ROS) storm generation, ferroptosis and apoptosis are significantly enhanced by FJP NCPs *in vivo*. In brief, this facile and efficient design for versatile nanoscale coordination polymers presents a novel paradigm for effectively elevating CDT efficiency and tumor synergistic therapy.

Recently, chemodynamic therapy (CDT) has been recognized as an attractive therapeutic modality to combat tumors by transforming overexpressed endogenous hydrogen peroxide (H_2O_2) into lethal hydroxyl radicals (·OH) through intratumoral Fenton-type reaction [1–3]. The generated ·OH is equipped to disrupt intracellular redox homeostasis and cause irreversible damage to organelles and DNA, eventually inducing cell death [4–6]. In comparison with photodynamic therapy and photothermal therapy, external excitation such as light in CDT procedure is not a requisite, which can availably surmount the restriction of the short-penetration depth of light and is more propitious to inhibit the growth of deeply located tumors [7,8]. Ferroptosis, which is characterized by the enhancement of oxidative stress, glutathione (GSH) consumption, lipid peroxidation (LPO) up-regulation, and suppression of lipid repair enzyme glutathione peroxidase 4 (GPX4), is considered to be a feasible and promising therapeutic tactic for tumor inhibition due to its potential to evade the inherent or induced resistance towards apoptosis and its collaborative involvement in CDT [9–11]. Mounting evidence demonstrates that the Fenton reaction has been implicated as an explicit mechanism to cause ferroptotic cell death [12–14]. The ·OH generated by the Fenton reaction can irrevocably trigger the peroxidation of membrane lipids, leading to LPO accumulation and the activation of ferroptosis [15,16]. Moreover, the surplus ·OH can attack and destroy GPX4 protein and subsequently result in the downregulation of GPX4, which also actuates LPO accumulation by impeding the conversion from lethal LPO to innoxious lipid alcohols [17]. Therefore, ferroptosis plays a significant synergistic role in CDT. However, the therapeutic output of CDT and ferroptosis might be severely restricted by factors including the limited amount of endogenous H_2O_2 as well as the high expression of antioxidant GSH at the tumor sites [18–21]. Accordingly, the construction of a CDT nanoagent that integrates the merits of efficient H_2O_2 supplement and synchronous exhaustion of intracellular GSH is still highly demanded.

* Corresponding authors.
E-mail addresses: mapa675@ciac.ac.cn (P. Ma), jlin@ciac.ac.cn (J. Lin).

https://doi.org/10.1016/j.cclet.2024.109626
1001-8417/

In CDT process, the main route for intracellular H_2O_2 self-provision is directly delivering exogenetic H_2O_2 or metal peroxides as the precursors of H_2O_2 [22–25]. Nevertheless, the ineluctable leakage of H_2O_2 or precursors in the process of delivery and the unsustainable H_2O_2 provision will dent their efficacy in CDT enhancement [26–28]. Thus, the CDT improvement associated with efficient H_2O_2 supplementation within tumor cells still faces challenges. To tackle this problem, various anticancer drugs have been exploited in CDT such as camptothecin [29,30], doxorubicin (DOX) [31,32], β-lapachone [22,33], and cinnamaldehyde [34,35], which are competent to boost intracellular H_2O_2 levels to enhance CDT efficiency. Furthermore, considering that GSH consumption plays an essential role in CDT enhancement, varieties of nanoplatforms with GSH consumption capability have been constructed for GSH exhaustion-enhanced CDT, such as iron metal-organic frameworks (MOFs) [36], iron-based layered double hydroxides (LDHs) [37], Fe_3O_4 [38], Prussian blue [39], MnO_2 nanocomposites [40], and so on. However, some CDT nanoplatforms may ineluctably undergo sophisticated synthetic routes, unsatisfactory drug loading capacity, premature leakage as well as the slow release of cargoes [41–43]. Therefore, it is extraordinarily significative but still remains challenges to design an uncomplicated, reliable, and efficient CDT agent with desirable loading capacity, GSH elimination capability as well as H_2O_2 amplification capability for combinational efficient cancer treatment.

Nanoscale coordination polymers (NCPs) based on the coordination of natural products and metal ion connectors have drawn considerable attention for CDT owing to their facile preparation, favorable biocompatibility, high drug loading capacity, and pH responsiveness [44–48]. Juglone (5–hydroxy-1,4-naphthoquinone) is a phenolic compound isolated from *Juglans regia* and has been identified as a promising drug candidate for cancer treatment [36,49–51]. Previous studies have manifested that the cancer-related suppressive effects of juglone are related to up-regulated H_2O_2 levels [52,53]. Besides, juglone is capable of depleting GSH through the Michael addition involving thiols on GSH and α,β-unsaturated ketones on juglone [54,55]. However, the poor solubility of juglone in aqueous solutions and the existing nanodrug delivery systems with complex synthetic routes and low drug loading capacity fairly limit its further application [36]. Herein, inspired by the background hereinbefore, this work designs the carrier-free Fe(III)-juglone nanoscale coordinated nanoparticles and modified with 1,2-distearoyl-*sn*–glycero-3-phosphoethanolamine conjugated polyethylene glycol (DSPE-PEG) (denoted as FJP NCPs) to disrupt intracellular redox homeostasis and fulfill a self-reinforced chemodynamic cancer treatment (Scheme 1). In response to GSH-rich and acidic TME, the Fe^{2+}/Fe^{3+}-guided Fenton reaction is activated, resulting in ·OH downstream and up-regulation of LPO. On the other hand, the simultaneously released juglone contributes to increasing H_2O_2 levels based on the juglone-mediated electron reduction cascade reaction, which facilitates the Fenton reaction and strengthens CDT efficiency to effectively induce apoptotic cell death. Additionally, the dual GSH consumption mediated by juglone and Fe^{3+} can reverse the insensitivity of cancer cells towards CDT and inactivate GPX4 *via* the Michael addition and oxidation–reduction reactions, thus causing LPO accumulation and evoking ferroptosis. Importantly, a remarkable therapeutic effect is achieved *via* the combination of enhanced CDT and ferroptosis *in vitro* and *in vivo*, indicating a promising strategy for the application of nanoscale coordination polymers in the field of enhanced CDT and ferroptosis.

As shown in Fig. 1a, FJ NCPs are fabricated by dropwise adding ethyl acetate into the mixture of $Fe(NO_3)_3{\cdot}9H_2O$ and juglone dissolved in dimethylformamide (DMF) solution and stirring vigorously at ambient temperature. Subsequently, FJ NCPs were modified with DSPE-PEG, which is designed to ameliorate the water solubility of nanoparticles, resulting in the formation of FJP

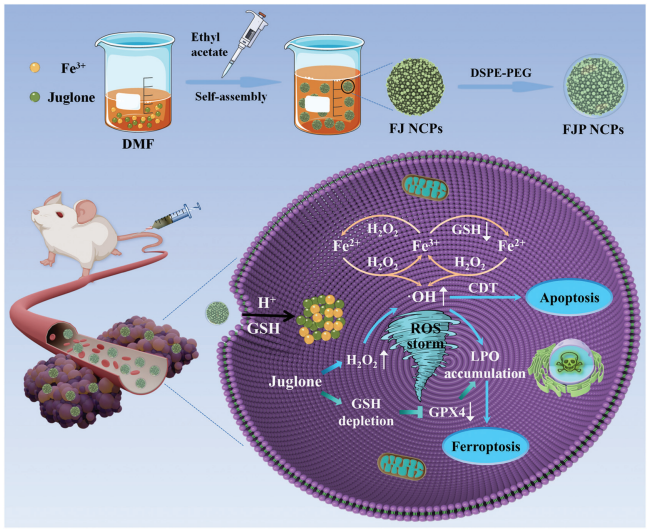

Scheme 1. Schematic illustration of the fabrication process and antitumor performance of FJP NCPs.

NCPs. The scanning electron microscopy (SEM) and transmission electron microscopy (TEM) observations confirm that FJP NCPs exhibit spherical-like morphology with a diameter of approximately 100 nm (Figs. 1b and c, Figs. S1 and S2 in Supporting information). The presence of juglone and Fe in FJP NCPs is demonstrated by the homogenous distributions of C, N, O, and Fe detected in element mappings, verifying the successful synthesis of FJP NCPs as designed (Fig. 1d). Moreover, the X-ray photoelectron spectroscopy (XPS) analysis distinctly presents the appearance of these above elements (Fig. S3 in Supporting information). The high-resolution XPS patterns of Fe 2p in FJP NCPs present two binding energy peaks at 711.4 and 725.0 eV, which could be assigned to Fe $2p_{3/2}$ and Fe $2p_{1/2}$ separately and indicate the presence of ferric iron species in FJP NCPs (Fig. 1e). The Fourier transform infrared (FTIR) spectra validate the formation of coordinated bonding between Fe^{3+} and the phenolic hydroxyl groups as well as carbonyl groups of juglone since the peak of C–O stretching vibration around 1222 cm^{-1} vanishes within FJP NCPs, and the characteristic peak of C=O stretching vibration in juglone significantly shifts from 1642 cm^{-1} to 1531 cm^{-1}. The bands of FJP NCPs at 3450 and 2917 cm^{-1} are allocated to DSPE-PEG, revealing the successful coating of DSPE-PEG to FJ NCPs (Fig. 1f). After the modification with DSPE-PEG, the average hydrodynamic diameter of FJP NCPs slightly increases from 120 nm to 140 nm, and the zeta potential changes from −10.1 eV to −14.6 eV, indicating the successful surface coating of DSPE-PEG (Figs. S4 and S5 in Supporting information). The powder X-ray diffraction (PXRD) patterns of the as-constructed FJP NCPs exhibit a broad hump after the strong coordination between juglone and Fe^{3+}, indicating the amorphous nature of FJP NCPs (Fig. S6 in Supporting information).

The drug loading capacity of juglone is evaluated to be as high as 77.4% ± 4.9% upon calculating by ultraviolet–visible (UV–vis) spectrum (Fig. S7 in Supporting information). In addition, with the increase of the ratio of Fe^{3+} to juglone, the drug loading capacity still remains above 70% (Fig. S8 in Supporting information). With a Fe content of 17.64% quantificationally assessed by inductively coupled plasma mass spectrometry (ICP-MS), correspondingly, the molar ratio of juglone to Fe^{3+} in FJ NCPs is determined as approximately 3/2 (Fig. S9 in Supporting information) [56]. The bright yellow color of juglone turns dark brown after mixing with Fe^{3+} (Fig. S10 in Supporting information). Correspondingly, the UV–vis absorption spectra of FJP NCPs show that the peak of juglone

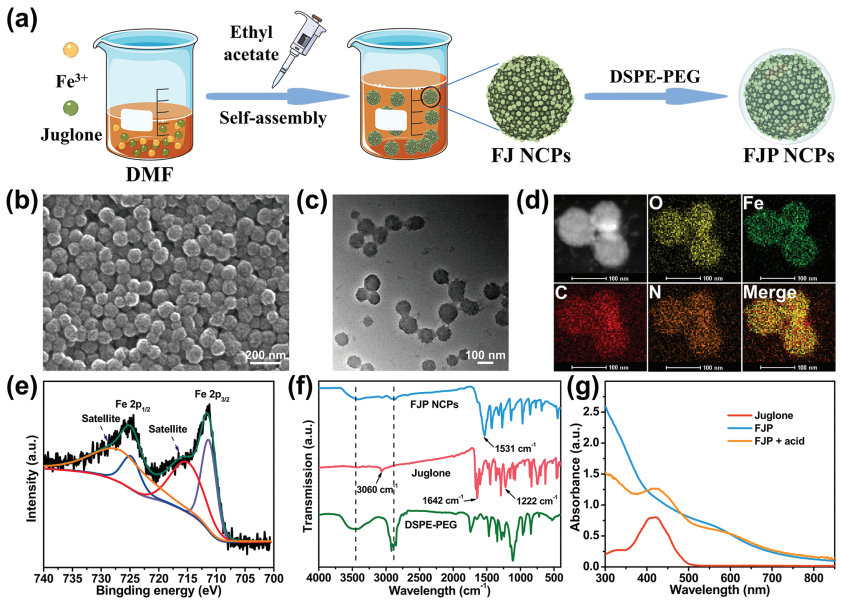

Fig. 1. The fabrication and characterization of FJP NCPs. (a) The synthesis and modification of FJP NCPs. (b) SEM images of FJP NCPs. (c) TEM images of FJP NCPs. (d) HAADF-STEM image and elemental mapping of FJP NCPs. (e) FTIR spectra of FJP NCPs, juglone, and DSPE-PEG. (f) Fe 2p XPS spectra of FJP NCPs. (g) UV–vis absorption spectra of juglone, FJP, and FJP + acid.

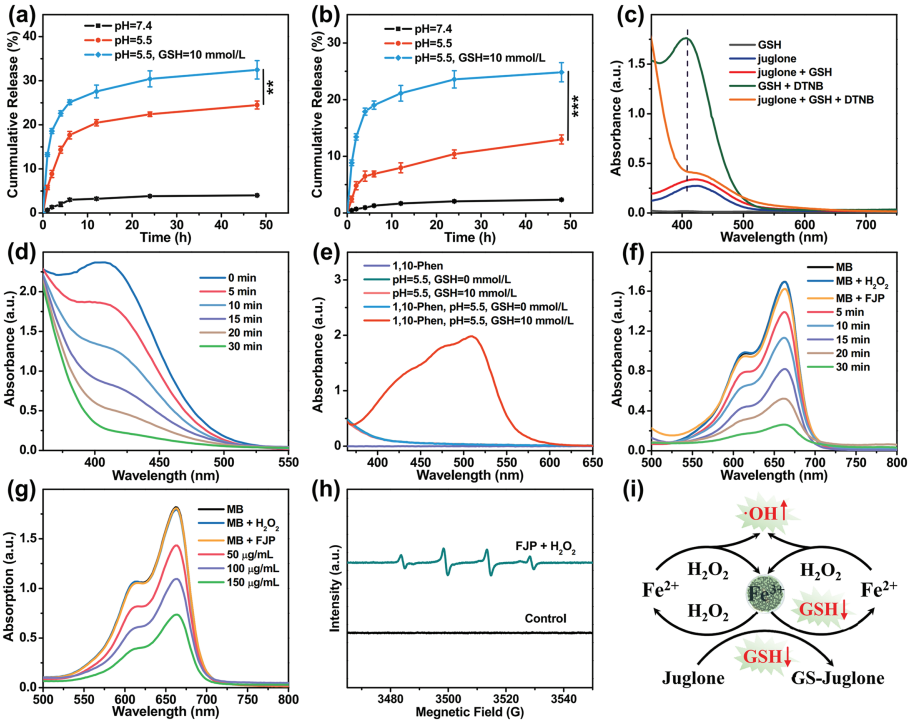

Fig. 2. (a) Juglone release profiles of FJP NCPs under different conditions. (b) Accumulative Fe release of FJP NCPs under different conditions ($n = 3$). Data are shown as mean ± standard deviation (SD); n represents the number of biologically independent samples. $^{**}P < 0.01$, $^{***}P < 0.001$. (c) GSH consuming ability of juglone. (d) GSH consuming ability of FJP at different times. (e) UV–vis spectra of 1,10-phenanthroline, FJP under pH 5.5 with or without GSH, and the mixture of 1,10-phenanthroline and FJP with or without GSH under pH 5.5. (f) UV–vis absorption spectra of MB degradation at different times. (g) UV–vis spectra of MB degradation under different concentrations of FJP. (h) ESR spectra of different groups by applying DMPO as the trapping agent. (i) Schematic illustration of the capability of producing ·OH and consuming GSH.

at 420 nm disappears after the coordination between juglone and Fe^{3+}. Additionally, the reemergence of the characteristic peak at about 420 nm is observed after adding acid into the FJP, indicating not only the successful complexation of juglone with Fe^{3+} in FJP NCPs but also the successful release of juglone under acidic conditions (Fig. 1g). To determine the drug release behavior of FJP NCPs under different conditions, the liberation of juglone and Fe^{3+} under incubation in different conditions is monitored by UV–vis spectrometry and ICP-OES, respectively. As depicted in Fig. 2a, less than 4.0% of juglone is liberated in neutral milieu (pH 7.4) even after 48 h, whereas the release of juglone at acidic condition (pH 5.5) is significantly higher than that in neutral environment, and a sharp release is observed from FJP incubated with GSH (10 mmol/L) at pH 5.5, suggesting a sensitive pH/GSH dual responsiveness of FJP in juglone release. In consistence with the juglone release behavior, 24.83% of Fe ions are released under double stimuli (pH 5.5,

GSH = 10 mmol/L) after 48 h, whereas only 2.34% of Fe ions are liberated in the neutral medium (Fig. 2b).

The substantial consumption of GSH overexpressed in tumor cells is capable of lessening the scavenging of reactive oxygen species (ROS) and effectively improving CDT outcomes. Then, the capability of juglone to consume GSH is examined by utilizing 5,5′-dithiobis(2-nitrobenzoic acid) (DTNB) as the probe with a characteristic peak centered at 412 nm [14]. As revealed in Fig. 2c, it can be seen that the GSH + DTNB group shows a specific peak at 412 nm, but the absorbance intensity at 412 nm decreases significantly in the juglone + GSH + DTNB group, implying that juglone efficaciously consumes GSH. With the prolonged treatment time, the absorbance of DTNB at 412 nm goes down gradually (Fig. 2d), and the reaction solution undergoes a noticeable color change from yellow to colorless (Fig. S11 in Supporting information), demonstrating the GSH consuming capability of FJP NCPs due to the reduction of Fe^{3+} and the Michael addition by juglone (Fig. S12 in Supporting information). Several small molecules or chemotherapeutic drugs have been reported to be used in GSH consumption through the Michael addition between thiols on GSH and α,β-unsaturated ketones on these molecules, including α-cyano-4-hydroxycinnamic acid [10], naphthazarin [11], cinnamaldehyde [31], gallic acid [57], and oxidized (−)-epigallocatechin-3-*o*-gallate [58], *etc*. In addition, 1,10-phenanthroline (1,10-phen), which reacts with Fe^{2+} to engender a colored $[Fe(phen)_3]^{2+}$ complex with a characteristic peak at 512 nm, is utilized for the detection of Fe^{2+} springing from the reduction of Fe^{3+} [34]. From Fig. 2e, FJP-treated 1,10-phen at pH 5.5 shows no striking absorbance at 512 nm, while an obvious absorption band at 512 nm is observed for GSH-treated FJP at pH 5.5. Moreover, there is a remarkable color change from transparent to orange, proving that Fe^{3+} has been reduced (Fig. S13 in Supporting information). After the addition of potassium ferricyanide rather than potassium thiocyanate, the color of the FJP supernatant treated with GSH transforms from light yellow to blue, indicating the existence of Fe^{2+} (Fig. S14 in Supporting information). The ·OH production capability of FJP NCPs is measured by selecting methylene blue (MB) as the indicator, which can be oxidized with an absorption peak at 664 nm from blue to achromatous [13]. As depicted in Figs. 2f and g, the absorption intensity of MB treated with FJP and H_2O_2 together gradually decreases with the prolongation of reaction durations and the increase of FJP concentration, and the blue color of the reaction solution gradually lightens (Fig. S15 in Supporting information). Furthermore, the electron spin resonance (ESR) spectra measurement, based on 5,5-dimethyl-1-pyrroline *N*-oxide (DMPO) as ·OH capture agent, also displays a detectable signal of ·OH (1:2:2:1) on treatment with FJP and H_2O_2 together(Fig. 2h). These results above preliminary reveal the valid GSH consumption and ·OH generation capacity of FJP NCPs, which presents a potential candidate for efficiently enhanced CDT (Fig. 2i).

We next examine the antitumor effect of FJP NCPs at the cellular level. The red emission gradually becomes stronger in treated mouse breast cancer cells (4T1 cells) with the extension of time, revealing the effective cell uptake of the FJP NCPs (Fig. S16 in Supporting information). A concentration-dependent cytotoxicity of FJP NCPs against 4T1 cells is observed, and the mortality rate of 4T1 cells incubated with 150 μg/mL of FJP NCPs is almost 78% (Fig. 3a). However, the survival rate of L929 cells is still above 90% under identical conditions (Fig. S17 in Supporting information), suggesting the desirable biocompatibility of FJP NCPs. It is considered that elevating intracellular H_2O_2 levels is a potentially valuable strategy to effectively engage CDT for the purpose of synergistic treatment [59]. Previous reports have revealed that juglone is capable of elevating intracellular H_2O_2 production through a redox cycle between oxidoreductase and quinones [36,60]. As displayed in Fig. S18 (Supporting information), the H_2O_2 levels increase with the juglone concentration increasing, resulting in cell death.

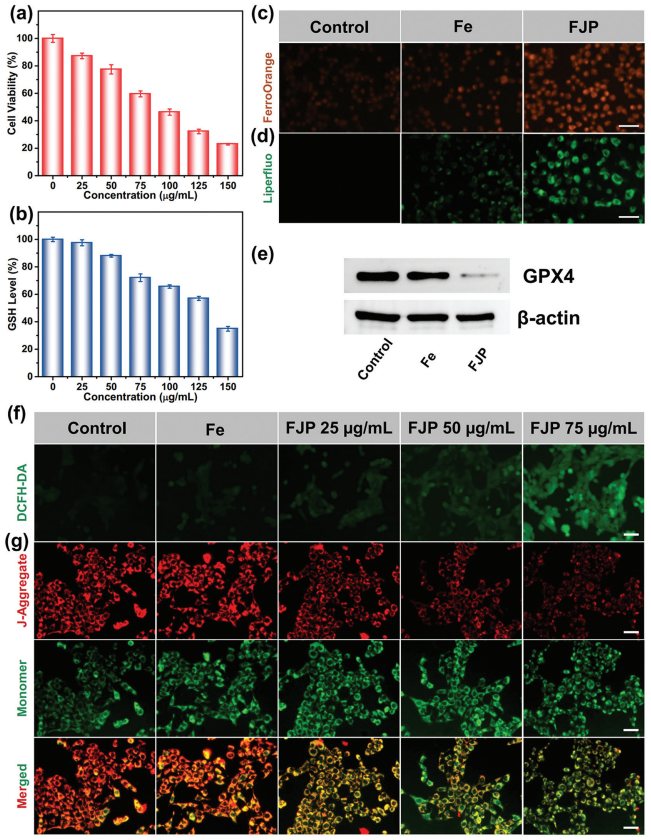

Fig. 3. (a) The cell viability of 4T1 cells after incubation with FJP NCPs at different concentrations for 24 h ($n = 3$). (b) Intracellular GSH consumption with different concentrations of FJP NCPs ($n = 3$). Data are shown as mean ± SD; n represents the number of biologically independent samples. (c) Fluorescence images of 4T1 cells stained with Fe^{2+} probe FerroOrange under different treatments. (d) Fluorescence observation for LPO measurement of 4T1 cells after various treatment. Scale bar: 20 μm. (e) GPX4 expression level of 4T1 cells treated with $Fe(NO_3)_3{\cdot}9H_2O$, and FJP NCPs. (f) Fluorescence images of 4T1 cells under various formulations and stained by DCFH-DA. (g) Fluorescence images of 4T1 cells after incubation with JC-1 probe under different treatments. Scale bar: 20 μm.

Due to a belief that GSH as the ·OH scavenger can markedly impede the CDT effects, a reduced GSH assay kit is utilized to determine the GSH consumption capacity of FJP NCPs [60–64]. As presented in Fig. 3b, the contents of GSH reduce dramatically with the increasing concentration of FJP NCPs, which is consistent with the outcomes of the DTNB degradation test. Furthermore, the GSH-depleted effects of FJP NCPs are also confirmed by an intracellular GSH probe (Thiol Tracker Violet). As displayed in Fig. S19 (Supporting information), FJP NCPs present notable GSH reduction with FJP concentration increasing, persuasively implying that FJP NCPs have the potential to exhaust intracellular GSH. Fig. 3c displays the intracellular Fe^{2+} levels by utilizing FerroOrange as the fluorescence probe. An obvious emission and the strongest fluorescence intensity are observed in the FJP-treated 4T1 cells, signifying the highest concentration of Fe^{2+} generated in the FJP group, consistent with the results of the 1,10-phenanthroline experiment. The enhancement in intracellular Fe^{2+} levels can hasten the Fenton reaction for ROS generation. Moreover, owing to the sufficient GSH consumption and superior ·OH production, the FJP group displays the strongest green emission detected by the Liperfluo probe, suggesting substantial LPO accumulation and the occurrence of ferroptosis (Fig. 3d). Since the GSH exhaustion and ROS accumulation directly disrupt the redox balance of 4T1 cells and further result

in the downregulation of GPX4, the activated CDT is expected to induce apoptotic and ferroptotic cell death. Inevitably, the GPX4 band in the FJP group is much weaker than that of the other groups, demonstrating the FJP-mediated effective ferroptosis (Fig. 3e and Fig. S20 in Supporting information). Collectively, the aforementioned results convincingly manifest that FJP NCPs can effectively induce ferroptotic cell death.

Investigated by 2′,7′-dichlorofluorescein diacetate (DCFH-DA), the fluorescence intensity in the FJP group apparently increases compared to those in the control group and Fe group with the FJP concentration increasing, which substantiates the massive accumulation of intracellular ROS in FJP group due to the enhanced CDT stemming from juglone (Fig. 3f). The result above indicates that the released juglone is equipped to destroy intracellular redox homeostasis by consuming GSH to dent the resistance of tumor cells to CDT, giving ·OH more opportunity to bring about serious impairment to DNA, protein, and lipids in tumor cells, thereupon ameliorating the CDT performance. Hence GSH consumption from juglone may occupy the most critical position than H_2O_2 elevation from juglone and ·OH generation from the Fenton reaction. Both ferroptosis and apoptosis are associated with mitochondrial dysfunction, which is manifested by the loss of mitochondrial membrane potential (MMP). The damage of mitochondria is validated by a decrease in MMP, as revealed by the transition of a potential-sensitive fluorescent indicator (JC-1) from red to green emission in a FJP concentration-dependent manner (Fig. 3g). Furthermore, the ROS production involving Fe^{3+}, Fe^{2+}, and juglone in FJP NCPs can result in the rupture of the lysosome membrane, which generally occurs at the early period of apoptosis. The gradually diminished red fluorescence with the increment of FJP concentration as examined by acridine orange (AO) staining assay reveals the manifestation of the destabilization and incompleteness of the lysosomal membrane (Fig. S21 in Supporting information). In addition, flow cytometry analysis is carried out to evaluate the curative effects of FJP NCPs. As illustrated in Fig. S22 (Supporting information), FJP NCPs elicit tumor cell death in a concentration-dependent manner, ulteriorly confirming that apoptotic cell death is also involved in synergetic therapy. Taken together, these abovementioned results unambiguously demonstrate that FJP NCPs can serve as a juglone delivery system, an iron ion source, as well as a potent CDT amplifier to efficaciously induce ferroptosis and apoptosis in 4T1 cells on account of the synergistic integration of ROS generation, GSH elimination, and triggered release of chemotherapeutic juglone.

The satisfactory *in vitro* curative effects of FJP NCPs stimulate us to explore their antitumor performance *in vivo* [5,6]. All animals in this study are handled according to a protocol approved by the Institutional Animal Care and Use Committee of Jilin University. The therapeutic efficacy of FJP NCPs is inspected on 4T1 subcutaneous tumor model of female BALB/c mice (Fig. 4a). The animal experiments agree with the criteria of The National Regulation of China for Care and Use of Laboratory Animals. As illustrated in Figs. 4b–d, the juglone group achieves moderate tumor growth inhibition. Comparatively, FJP NCPs remarkably inhibit tumor growth, and the minimal tumor volume and the lightest tumor weight are observed in the FJP group among these four groups, which could be assigned to the reinforced CDT and ferroptosis. To detect the antitumor treatment efficacy from the perspective of histological level, several types of staining are performed on tumor histopathological sections (Fig. 4e). The hematoxylin and eosin (H&E) staining results of tumor tissues manifest bulky cavities and mountains of overflowing cytoplasm in the FJP-treated group, in consistence with tumor growth data. Simultaneously, the terminal deoxynucleotidyl transferase-mediated dUTP nick-end labeling (TUNEL) staining sections also illustrate that FJP NCPs cause severe cell apoptosis in the higher level in comparison to other formulations, testifying the notable tumor inhibitory effects of FJP NCPs. In consideration of

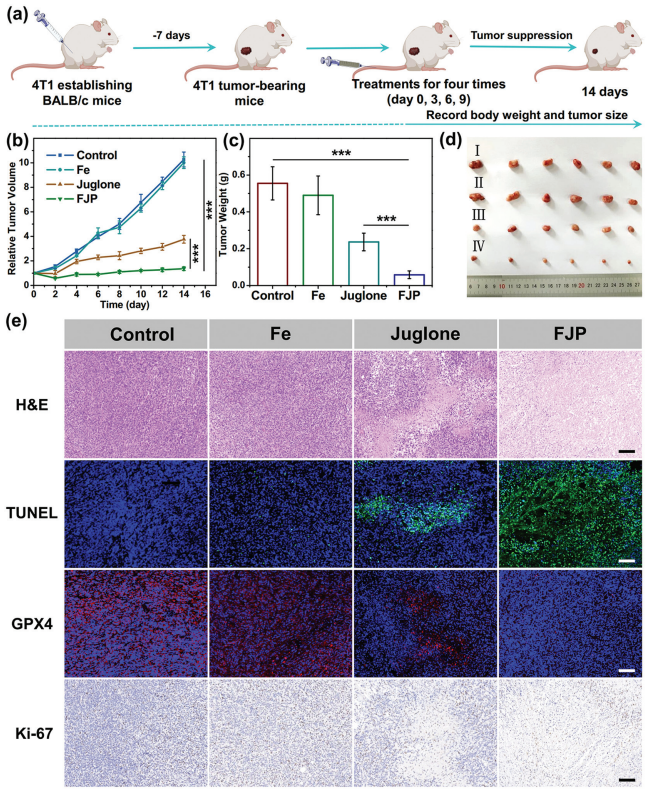

Fig. 4. (a) Schematic illumination of 4T1 tumor heterograft and treatment outcomes of FJP NCPs. (b) The relative tumor volume growth curves of tumor-bearing mice after different treatments ($n = 3$). $^{***}P < 0.001$. (c) The average tumor weight from sacrificed mice at the end of different treatments ($n = 6$). Data are shown as mean ± SD; n represents the number of biologically independent samples. (d) Representative photograph of the dissected tumors on day 14 after various treatments (I. Control; II. $Fe(NO_3)_3{\cdot}9H_2O$; III. Juglone; IV. FJP). (e) H&E, TUNEL, GPX4, and Ki-67 staining results of tumor biopsies obtained from tumor-bearing mice after 14 days of various treatments. Scale bar: 100 μm.

the essentiality of GPX4 in GSH exhaustion-mediated ferroptosis, the immunofluorescence staining of GPX4 protein in tumor specimens after different treatments is further assessed. The expression of GPX4 in tumor cells subjected to FJP treatment witnesses a noticeable down-regulated tendency, suggesting the occurrence of ferroptosis. Consistently, in virtue of tumor tissue impairment, the FJP group displays much suppressed proliferation capacity as can be observed in Ki-67 sections. Collectively, the FJP NCPs are capable of orchestrating the enhanced CDT and ferroptosis synergistically, which leads to a superior therapeutic effect *in vivo*. Noteworthy, the body weights in the FJP group display acceptable fluctuations during the therapeutic period, while mice in the juglone group show a visible loss of body weight, which is ascribed to the systematic toxicity of free juglone (Fig. S23 in Supporting information). Moreover, the H&E staining results of the major organs disclose inconspicuous pathological lesions after treatment with FJP NCPs, whereas there are observable abnormalities in the liver slice of the juglone group (Fig. S24 in Supporting information), implying that the coordinated self-assembly between juglone and Fe^{3+} into FJP NCPs can bring down the adverse side effects of juglone, thus validating the desirable biosafety of the TME-responsive FJP NCPs.

In summary, we elaborately fabricated a TME-responsive ROS storm nanogenerator based on the coordinated self-assembly between Fe^{3+} and juglone, which could achieve high antitumor efficiency by inducing ferroptosis and apoptosis. Synergizing ROS storm was realized by a self-reinforced CDT on the basis of the increasing endogenous H_2O_2 supplied by juglone as well as the re-

leased Fe^{2+}/Fe^{3+} flow. Additionally, the dual GSH depletion strategy achieved by the reduction of Fe^{3+} as well as the Michael addition reaction between juglone and GSH significantly caused the GPX4 inactivation and LPO accumulation, in turn evoking effective ferroptotic cell death. This work not only reveals the orchestrated multifunctional treatment of FJP NCPs towards tumor cells but also paves new avenues for the application of nanoscale coordination polymers in the field of enhanced CDT and ferroptosis.

Declaration of competing interest

The authors declare that they have no known competing financial interests or personal relationships that could have appeared to influence the work reported in this paper.

Acknowledgments

This work is financially supported by the National Key Research and Development Program of China (No. 2022YFB3503700), the National Natural Science Foundation of China (NSFC, Nos. 51929201, 52102354, and 52202353), the projects for science and technology development plan of Jilin province (Nos. 20220101070JC, 20210402046GH, and 20220508089RC).

Supplementary materials

Supplementary material associated with this article can be found, in the online version, at doi:10.1016/j.cclet.2024.109626.

References

[1] P.R. Zhao, H.Y. Li, W.B. Bu, Angew. Chem. Int. Ed. 62 (2023) e202210415.
[2] Z.M. Tang, Y.Y. Liu, M.Y. He, W.B. Bu, Angew. Chem. Int. Ed. 58 (2019) 946–956.
[3] C. Zhang, W.B. Bu, D.L. Ni, et al., Angew. Chem. Int. Ed. 128 (2016) 2141–2146.
[4] J.Y. Lu, Y.Q. Yang, Q.Q. Xu, et al., Coord. Chem. Rev. 474 (2023) 214861.
[5] X.M. Zhang, S. Lin, F. Zhao, et al., Adv. Mater. 35 (2023) 2210876.
[6] J. Wang, H.Y. Ding, Y. Zhu, et al., Angew. Chem. Int. Ed. 62 (2023) e202302255.
[7] Y.L. Wu, Y.L. Li, G.L. Lv, W.B. Bu, Chem. Sci. 13 (2022) 2202–2217.
[8] H.Y. Gao, Z.P. Cao, H.H. Liu, et al., Theranostics 13 (2023) 1974–2014.
[9] L.F. Ma, H. Huang, W. Feng, et al., Adv. Funct. Mater. 32 (2022) 2208220.
[10] Q. Meng, J. Tan, W.F. Tong, et al., Chem. Eng. J. 471 (2023) 144563.
[11] Z.D. Liu, S.N. Liu, B. Liu, et al., Small 19 (2023) 2207825.
[12] G. Lei, L. Zhuang, B.Y. Gan, Nat. Rev. Cancer 22 (2022) 381–396.
[13] S.J. Dixon, K.M. Lemberg, M.R. Lamprecht, et al., Cell 149 (2012) 1060–1072.
[14] K.X. Liu, L. Huang, S.Y. Qi, et al., Adv. Healthc. Mater. 12 (2023) 2203085.
[15] C. Liang, X.L. Zhang, M.S. Yang, X.C. Dong, Adv. Mater. 31 (2019) 1904197.
[16] Z.Y. Shen, J.B. Song, B.C. Yung, et al., Adv. Mater. 30 (2018) 1704007.
[17] Z.C. Zhang, Y.W. Ding, J.B. Li, et al., Nano Res. 14 (2021) 2398–2409.
[18] C.H. Liu, Y. Cao, Y.R. Cheng, et al., Nat. Commun. 11 (2020) 1735.
[19] B.Y. Niu, K.X. Liao, Y.X. Zhou, et al., Biomaterials 277 (2021) 121110.
[20] Y.X. Xiong, C. Xiao, Z.F. Li, et al., Chem. Soc. Rev. 50 (2021) 6013–6041.
[21] Y. Cao, S. Zhang, Z.J. Lv, et al., Adv. Funct. Mater. 32 (2022) 2209227.
[22] X.J. Zhang, C.C. He, Y. Chen, et al., Biomaterials 275 (2021) 120987.
[23] S.T. Gao, Y. Jin, K. Ge, et al., Adv. Sci. 6 (2019) 1902137.
[24] L.S. Lin, T. Huang, J.B. Song, et al., J. Am. Chem. Soc. 141 (2019) 9937–9945.
[25] J. Liu, W.X. Yang, Y.Q. Huang, et al., Nano Res. 16 (2023) 7134–7147.
[26] L.H. Fu, Y.L. Wan, C. Qi, et al., Adv. Mater. 33 (2021) 2006892.
[27] M. Wang, D.M. Wang, Q. Chen, et al., Small 15 (2019) 1903895.
[28] C. Yang, M.R. Younis, J. Zhang, et al., Small 16 (2020) 2001518.
[29] D.M. Zhu, H. Chen, C.Y. Huang, et al., Adv. Funct. Mater. 32 (2022) 2110268.
[30] W.T. Zhang, C. Liu, Z.W. Liu, et al., ACS Nano 16 (2022) 20975–20984.
[31] Z.Z. Zhang, Y. Pan, J.E. Cun, et al., Acta Biomater. 151 (2022) 480–490.
[32] J.D. Lin, H.K. Yang, Y.X. Zhang, et al., Small 19 (2023) 2205024.
[33] J.E. Cun, Y. Pan, Z.Z. Zhang, et al., Biomaterials 287 (2022) 121687.
[34] L.W. Wang, X.D. Zhang, Z. You, et al., Angew. Chem. Int. Ed. 62 (2023) e202217448.
[35] Y. Bai, Y.J. Pan, N. An, et al., Chin. Chem. Lett. 34 (2023) 107552.
[36] L. Zhao, Z.X. Li, J.J. Wei, et al., Chem. Eng. J. 430 (2022) 133057.
[37] X.T. Yang, L. Wang, S.T. Guo, et al., Adv. Healthc. Mater. 10 (2021) 2100539.
[38] F. Wu, C.G. Huang, B.H. Sun, et al., ACS Sustain. Chem. Eng. 10 (2022) 6346–6357.
[39] S.Q. Guan, X.J. Liu, Y. Fu, et al., J. Colloid Interface Sci. 608 (2022) 344–354.
[40] S.Q. Guan, X.J. Liu, C.L. Li, et al., Small 18 (2022) 2107160.
[41] K.K. Yang, G.C. Yu, Z.Q. Yang, et al., Angew. Chem. Int. Ed. 60 (2021) 17570–17578.
[42] Y.L. Dai, Z. Yang, S.Y. Cheng, et al., Adv. Mater. 30 (2018) 1704877.
[43] P.A. Ma, H.H. Xiao, C. Yu, et al., Nano Lett. 17 (2017) 928–937.
[44] S.S. Garcia, R. Solorzano, R. Alibes, et al., Coord. Chem. Rev. 441 (2021) 213977.
[45] Y.H. Liu, S.B. Lv, D.P. Liu, F.L. Song, Acta Biomater. 116 (2020) 16–31.
[46] S. Liu, X.P. Xu, J. Ye, et al., Chem. Eng. J. 456 (2023) 140892.
[47] J.T. Xu, J. Wang, J. Ye, et al., Adv. Sci. 8 (2021) 2101101.
[48] W. Jung, D.Y. Lee, E. Moon, S. Jon, Adv. Drug Deliv. Rev. 191 (2022) 114620.
[49] J. Wang, K. Liu, X.F. Wang, D.J. Sun, Oncol. Rep. 38 (2017) 1959–1966.
[50] Y.Y. Zhang, Z.J. Ni, E. Elam, et al., Food Funct. 12 (2021) 4947–4959.
[51] J.F. Du, K. Krishnamoorthy, V. Ramabhai, D.X. Yang, Mol. Biotechnol. 66 (2024) 1071–1081.
[52] P. Wang, S.D. Zhang, J. Jiao, et al., Toxicol. Appl. Pharm. 379 (2019) 114647.
[53] T. Ahmad, Y.J. Suzuki, Antioxidants 8 (2019) 91.
[54] A. Bohme, D. Thaens, F. Schramm, A. Paschke, G. Schuurmann, Chem. Res. Toxicol. 23 (2010) 1905–1912.
[55] Y.T. Dong, Q. Jin, L. Zhou, J. Chen, Org. Lett. 18 (2016) 5708–5711.
[56] W.J. Feng, W.R. Shi, S.W. Liu, et al., Adv. Healthc. Mater. 11 (2022) 2101926.
[57] F. Zhao, H.Y. Yu, L.Y. Liang, et al., Adv. Healthcare Mater. 12 (2023) 2301346.
[58] W.Y. Zhen, Y. Liu, S.J. An, X.E. Jiang, Angew. Chem. Int. Ed. 62 (2023) e202301866.
[59] S.M. Dong, Y.S. Dong, B. Liu, et al., Adv. Mater. 34 (2022) 2107054.
[60] J.J. Inbaraj, C.F. Chignell, Chem. Res. Toxicol. 17 (2004) 55–62.
[61] L.P. Dong, J.S. Ding, L.M. Zhu, et al., Chin. Chem. Lett. 34 (2023) 108192.
[62] F.W. Sun, Y.Y. Peng, Y.P. Li, M.H. Xu, T. Cai, Chin. Chem. Lett. 34 (2023) 107157.
[63] M.F. Wang, P.A. Ma, L. Lin, Chin. Chem. Lett. 34 (2023) 108300.
[64] X.C. Li, R. Luo, X.Q. Liang, Q.J. Wu, C.Y. Gong, Chin. Chem. Lett. 33 (2022) 2213–2230.